NeuroImage 147 (2017) 152–163

Contents lists available at ScienceDirect

NeuroImage

journal homepage: www.elsevier.com/locate/neuroimage

Studying cyto and myeloarchitecture of the human cortex at ultra-high field with quantitative imaging: R_1, R_2^* and magnetic susceptibility

José P. Marques[a,*,1], Diana Khabipova[a,b,1], Rolf Gruetter[b,c,d]

[a] Donders Centre for Cognitive Neuroimaging, Radboud University, Nijmegen, Netherlands
[b] Laboratory for Functional and Metabolic Imaging, Ecole Polytechnique Fédérale de Lausanne, Lausanne, Switzerland
[c] Department of Radiology, University of Geneva, Geneva, Switzerland
[d] Department of Radiology, University of Lausanne, Lausanne, Switzerland

ABSTRACT

In this manuscript, the use of quantitative imaging at ultra-high field is evaluated as a mean to study cyto and myelo-architecture of the cortex. The quantitative contrasts used are the longitudinal relaxation rate (R_1), apparent transverse relaxation rate (R_2·) and quantitative susceptibility mapping (QSM).

The quantitative contrasts were computed using high resolution in-vivo (0.65mm isotropic) brain data acquired at 7 T.

The performance of the different quantitative approaches was evaluated by visualizing the contrast between known highly myelinated primary sensory cortex regions and the neighbouring cortex. The transition from the inner layers to the outer layers (from white matter to the pial surface) of the human cortex, which is known to have varying cyto- and myelo architecture, was evaluated.

The across cortex and through depth behaviour observed for the different quantitative maps was in good agreement between the different subjects, clearly allowing the differentiation between different Brodmann regions, suggesting these features could be used for individual cortical brain parcellation. While both R_1 and R_2^* maps decrease monotonically from the white matter to the pial surface due to the decrease of myelin and iron between these regions, magnetic susceptibility maps have a more complex behaviour reflecting its opposing sensitivity to myelin and iron concentration.

1. Introduction

The study of cortical brain structure has been an important field of research for the last century. In the beginning of the twentieth century, the cytostructure and myelostructure were studied in ex vivo samples using the Nissl and Weissl stain method to unveil the cytostructure (Brodmann, 1909; Sarkissov et al., 1955; von Economo and Koskinas, 1925) and the myelostrucucture (Hopf and Gräfin Vitzthum, 1957; Vogt and Vogt, 1919) of the human cortex. Under the assumption that delimited regions with similar cyto- and myeloarchitecture would lead to specific functions, these groups parcellated the cortex of the human brain into regions, which can be further specified into areas and subareas, with the most well know parcellation being that suggested by Brodmann. Modern histology has evolved and new methods have been developed to study the cyto- and myeloarchitecture in a more specific and quantifiable way, e.g. immunohistochemistry and receptor mapping (Toga et al., 2006; Zilles et al., 2002; Zilles and Amunts, 2009). Also many analytical techniques are used to analyse the elementary composition of the tissue such as synchrotron X-ray fluorescence (XRF), proton-induced X-ray emission mapping (PIXE), inductively coupled plasma mass spectrometry (ICPMS) as well as atomic absorption spectrometry measurements (Hopp et al., 2010; Langkammer et al., 2012; McRae et al., 2009; Morawski et al., 2005; Stüber et al., 2014; Zheng et al., 2013).

During most of the 20th century, the understanding of human brain function heavily relied on clinical cases of brain injuries (Cramer et al., 2011; Kleist, 1937; Zilles and Amunts, 2010). The development of functional brain imaging techniques such as positron emission tomography (PET) in a first instance and later functional magnetic resonance imaging (fMRI) allowed neuroscientists to study the brain regions or networks associated with a given task, or even during rest, both in normal and pathological subjects. Although functional MRI and diffusion weighted imaging have had a huge role in the study of human brain function and connectivity, both at the group and individual level,

* Correspondence to: Donders Centre for Cognitive Neuroimaging, Kapittelweg 29, 6525 EN Nijmegen, The Netherlands.
E-mail address: j.marques@donders.ru.nl (J.P. Marques).
[1] These authors have contributed equally for the work presented in this manuscript.

http://dx.doi.org/10.1016/j.neuroimage.2016.12.009
Received 6 May 2016; Accepted 5 December 2016
Available online 07 December 2016
1053-8119/ © 2016 Elsevier Inc. All rights reserved.

there is still interest in being able to, with high spatial resolution, find anatomical landmarks that are associated with cortical structure that go beyond the simple observation of the cortical folding. Standard weighted imaging has long been shown to be able to visualize, locally, differences in cortical structure (Duyn et al., 2007). The first reports showing whole brain cortical maps where the differential properties of sensory and motor cortices in respect to surrounding tissue could be seen, have been obtained over 10 years ago by Fischl et al. (2002, 2004) yet, standard weighted imaging suffers from strong inhomogeneous bias fields associated with the RF transmission and reception that can bias comparisons between distant cortical regions. Only recently though has this field had a renovated attention thanks to the first reports suggesting that by combining T_1-weighted and T_2-weighted images, a myelin sensitive map could be obtained where cortical areas (matching published probabilistic cytoarchitectonically defined regions) could be delineated. The ratio T_1w/T_2w improves not only the contrast of heavily and lightly myelinated areas but also removes some MR-related intensity bias fields (Glasser and Essen, 2011). However, this ratio based method remains sensitive to the B_1 transmit field inhomogeneity, which contaminates comparisons of different subjects, scanners and facilities with different protocols.

An alternative to this phenomenological ratio is the use of MR quantitative methods such as longitudinal and apparent transverse relaxivity (R_1 and R_2*). Quantitative maps are independent of the specific hardware (other than field strength), its values are reproducible and depend only on the underlying tissue sub-structure originating the contrast rather than depending on effects such as transmit and receive B_1 field inhomogeneities. Various studies have shown a direct relationship between R1 and myelin content (Bot et al., 2004; Mottershead et al., 2003; Schmierer et al., 2004). Particularly in the human cortex, R_1 variations reflect water mobility (Bock et al., 2009; Geyer et al., 2011; Sigalovsky et al., 2006), yet the impact of iron content on R_1 tissue contrast should not be fully neglected (Rooney et al., 2007). This has now been clearly demonstrated in a recent ex-vivo study showing that it is beneficial to think of R_1 in grey and white matter to have a multivariate dependence on both myelin and iron concentration (Stüber et al., 2014). In vivo R_1 and R_2^* maps in the cortex show increased relaxation rates in primary Brodmann regions (Cohen-Adad et al., 2012; Sereno et al., 2013). Other than the ability to distinguish Brodmann areas, the study by Cohen-Adad et al. also observed that, within each region, there was a small dependence on the orientation of the cortical surface in respect to the magnetic field, suggesting that, in part, this contrast is not only modulated by iron load but is also due to the structurally organized myelin bundles running through the cortex. The same group has extended their analysis to include not only T_2^* cortical maps acquired at 7 T but also magnetization transfer ratio (MTR) obtained at 3 T and created “combined myelin estimation” maps (Mangeat et al., 2015). When looking exclusively at cortical R_1 maps, it was observed that the boundaries obtained using R_1 maps were in good agreement with those obtained using functional imaging to define on a single subject basis V1, MT (Sereno et al., 2013) and the auditory cortex (Dick et al., 2012). Such observations of similarity between the structural and functional observations have further recently culminated in the creation of a multimodal cortical parcellation of the human brain using both structural and resting state functional data (Glasser et al., 2016).

Inhomogeneities caused by para- or diamagnetic perturbers, such as iron and myelin, lead to a dephasing of nearby protons (Haacke et al., 2005), increasing their apparent transverse relaxation rate. Such processes are responsible for the clear delineation of veins, hypo intensities in deep gray matter structures and even the contrast between different white matter fibers in standard T_2^* weighted imaging. Instead, in quantitative susceptibility mapping (QSM) paramagnetic and diamagnetic entities, like iron and myelin, have opposing effects - reflecting the local induced magnetisation. However, to compute susceptibility maps from measured frequency shift maps, many pre-processing steps need to be performed, making cortical measurements difficult. The first step is to remove the background field from the measured field. A mask delineating the region of the local effects of interest has to be defined. Many background-correction methods presented in literature will either end up eroding this mask (losing relevant information on outer parts of the brain) or giving values that are unreliable close to the boundary, for an illustrated comparison of many of these methods refer to (Schweser et al., 2016). The second step is the calculation of the QSM from the measured field maps (after background field removal). This is an ill-posed problem that has been tackled by various groups (Wang and Liu, 2015). Despite these advances the most robust method to perform QSM is still the originally proposed over-determination of the problem by measuring the subject's head at different orientations in respect to the main magnetic field (Liu et al., 2009; Marques and Bowtell, 2005; Wharton et al., 2010) even if it is clear that there are limitations to the forward model used.

Iron concentration in deep gray matter structures (globus pallidus, putamen, caudate) have been shown to have a correlation with susceptibility (Bilgic et al., 2012; Langkammer et al., 2012; Lim et al., 2013; Schweser et al., 2011; Wharton and Bowtell, 2013, 2010). Myelin content does contribute to the gray and white matter contrast in phase imaging (C. Liu et al., 2011; Lodygensky et al., 2012) yet, not only is the myelin susceptibility anisotropic, its contribution to the measured phase images is driven by the microstructural compartmentalization of lipid organization and its orientation in respect to the static magnetic field (He and Yablonskiy, 2009; Luo et al., 2014; Wharton and Bowtell, 2013; Yablonskiy et al., 2012). These mechanisms are not taken into account in the COSMOS formalism, but they should only be dominating factors in regions where tissue is highly anisotropic (unlike grey matter).

The aim of this study is to evaluate the potential of using R_1, R_2^* and QSM to study myelo and cyto-architecture of the human brain. The reproducibility of the obtained quantitative cortical maps across subjects and the ability to identify spatial features suggestive of Brodmann areas were evaluated. Furthermore, the cortex was studied in its transition from its inner (border between gray matter (GM) – white matter (WM)) to the outer surface (border between gray matter (GM) - cerebrospinal fluid (CSF), pial surface). This “through depth behaviour” of the brain cortex was evaluated for all quantitative contrasts in regions of interest based on the Brodmann atlas, both at the individual and group level. The R1, R_2^* and susceptibility distributions across the cortex were used to attempt the calculation of cortical maps of myelin and iron distribution.

2. Methods

2.1. Data acquisition

Six healthy volunteers with ages ranging from 20 to 37 years (mean=27y) were scanned according to a protocol approved by the local ethics committee. Scans were performed on a 7 T MR scanner (Siemens, Erlangen, Germany) equipped with a head insert gradient, using single channel head only birdcage for RF transmission and a 32 channel receive coil for reception (Nova Medical).

2.1.1. R_1maps

The R_1-maps were acquired using the MP2RAGE (Marques et al., 2010) sequence. The sensitivity of the R_1 map estimation from the measured MP2RAGE to B_1^+ field inhomogeneities increases with the number of excitations per MP2RAGE repetition time. To overcome this problem the B_1^+ field was measured separately with the SA2RAGE sequence (Eggenschwiler et al., 2012). Subsequently the two datasets were used to compute a high resolution, full brain and bias field free R_1 maps (Marques and Gruetter, 2013).

The MP2RAGE and the SA2RAGE are closely related sequences in which two GRE images are acquired after a preparation pulse, either an

adiabatic inversion or a saturation pulse, and the timing of these acquisitions (named as TI – inversion time and TD – delay time depending on the preparation pulse used) determines their sensitivity to R_1 and transmit B_1.

The SA2RAGE acquisition had the following parameters: TR/TD_1/TD_2=2.4/0.045/1.8 s; BW=1200 Hz/Px; ; α_1/α_2=4°/10°; spatial resolution=2.2×2.2×2.0 mm^3; iPAT=3×1;Tacq=1 min 55 sec.

The MP2RAGE parameters were the following: TR/TI_1/TI_2=6/0.8/2.7 s; BW=300 Hz/Px;α_1/α_2=FA(α1/α2) = 7°/5°; spatial resolution=0.6×0.6×0.6 mm^3; Tacq=10 min 25 sec.

2.1.2. R_2^* and susceptibility maps

To retrieve the quantitative maps of the R_2^* and susceptibility, a standard 3D gradient echo multi echo sequence was used. The five acquired echoes were equally spaced and acquired with the same polarity gradients, the rewinding waveform was kept equal to the readout gradient waveform to ensure flow compensation between successive echoes along the readout direction (where the continuous switching of gradients would create the largest first gradient moments). The following parameters were used: TR/TE_1/ TE_5=42/4.97/37.77 ms, echo spacing=8.2 ms; bandwidth (BW)=260 Hz/Px; flip angle (FA)=10°, FOV=256x192×137 mm^3, spatial resolution 0.66×0.66×0.66 mm^3; iPAT=2×2;acquisition time (T_{acq})=11 min.

The protocol was repeated four times for each volunteer with different head positions: normal; head tilted around medio-lateral axis (left–right axis, pitch) in head-to-chest direction (up to 14°) position; tilted around anterior-posterior axis (roll) in head-to-left-shoulder direction (up to 25°) and head-to-right-shoulder direction (up to 25°). The subjects were removed from the scanner bore at the end of each scan, the subjects' head was re-positioned by the experimenter and was carefully cushioned to ensure comfort and minimise motion artefacts. A two step co-registration pipeline was used: first the magnitude images pre-brain extraction were co-registered (using a 12 parameters) to the normal head position; brain extraction was then applied and a final co-registration was then conducted (as detailed in Khabipova et al. (2015)). The exact head rotations were determined by combining the co-registration matrices obtained using FLIRT (www.fmrib.ox.ac.uk). No field map based spatial undistortion was used to account for the different spatial deformations at each head position because of the high BW per pixel in these acquisitions.

2.2. Data processing

All data processing was performed in MATLAB (version 2010b, The MathWorks, Natick, MA, USA) on a workstation (2xIntel Xeon X5650) with 96 GB RAM.

2.2.1. R_1 calculation

First, the low resolution SA2RAGE image with proton density contrast was co-registered to the high resolution MP2RAGE image with proton density contrast using FLIRT (www.fmrib.ox.ac.uk/fsl), the rotation matrix was then applied to the SA2RAGE ratio image. Lookup tables were used to relate each pixel of the SA2RAGE ratio image to their B_1^+ values assuming an initial estimation of tissue R1=0.67 s^{-1}. This B_1^+ value was used, with a lookup table, to estimate the R_1 value of a certain pixel of the MP2RAGE ratio image (Marques et al., 2010). The B1 estimation was then refined taking into account the new R_1 estimations. This process was repeated three times, at which point variations were shown to be negligible (Marques and Gruetter, 2013).

2.2.2. R_2* Map and susceptibility calculation

The multi-echo GRE data from the different coils were combined using pixel by pixel SVD decomposition of the channel by echo time matrix, field maps were obtained by using pixel by pixel SNR weighting (Khabipova et al., 2015) and R_2^* map were calculated using signal, S, decay integration over the number of echo times, nTE,

$$R_2^* = \frac{S_1 - S_{nTE}}{\sum_{i=1}^{nTE-1} 0.5(S_i + S_{i+1})\Delta TE} \quad (1)$$

The limited range of echo times used (short compared to the T2* of CSF) makes the calculation of R_2* values of CSF prone to noise amplification. To avoid that noise in the CSF or large pial veins could bleed into neighbouring cortical regions either during the co-registration or the surface extraction processes, pixels whose T^*_2 values were outside the range [0.33TE_1, 3TE_5] were attributed to the closest boundary value.

In order to retrieve the magnetic field map generated only by the local tissue sources, the EAHF (Efficient and Automatic Harmonic Field Pre-Filtering) background field removal was applied (de Rochefort et al., 2013). In the EAHF, the background filtered field map, δB_{in} (resulting from internal sources only), is computed by minimizing:

$$min_{\delta Bin} \| W_\Delta(\Delta\delta B - \Delta\delta B_{in}) \|, \quad (2)$$

where δB is the measured field and the Laplacian operator, Δ, used can be represented by the following 3×3×3 matrix:

$$\Delta = \begin{bmatrix} 0 & 0 & 0 \\ 0 & 1 & 0 \\ 0 & 0 & 0 \end{bmatrix} \begin{bmatrix} 0 & 1 & 0 \\ 1 & -6 & 1 \\ 0 & 1 & 0 \end{bmatrix} \begin{bmatrix} 0 & 0 & 0 \\ 0 & 1 & 0 \\ 0 & 0 & 0 \end{bmatrix} \quad (3)$$

applied by finite difference. To ensure a robust brain mask for all subjects, the original brain mask obtained with BET was eroded by two pixels. The boundary condition was then introduced by setting a mask, W_Δ, where the Laplacian values are trustworthy, which was obtained by eroding one extra pixel from the brain mask, and modulating it by the SNR of the measured field map.

Quantitative susceptibility maps were calculated using the COSMOS method (Liu et al., 2009) using the four different head orientations. No explicit reference region was used, the fields were made to have a zero mean value inside the brain mask and the average susceptibility in the whole volume was assumed to be zero.

2.3. Cortical maps

The magnitude contrast of the GRE acquisition was first co-registered to the R1 map using FSL-FLIRT. This registration matrix was then used to transform all quantitative contrasts (R1, R_2^* and susceptibility) to the same subject-space (as shown in Fig. 1).

In the next step the cortical surfaces of the gray-white matter border and GM-CSF border (pial) were retrieved from the common FreeSurfer software pipeline. These surfaces were used to compute equi-volume cortical surface layers from R_1 maps (Kleinnijenhuis et al., 2015) by sampling the surface vertices in steps of 20% of cortical volume (0% - depth 1 - grey-white matter surface, 100% - depth 6 - pial surface) across the entire cortical hemisphere without using any smoothing. These surfaces at different cortical depths were applied to χ and R_2^* maps to obtain the corresponding cortical maps. The pial surface was excluded from the remaining analysis because the quantitative maps of CSF have a large uncertainty and hence the pixels where CSF has a larger partial volume will be less reliable. In the remaining layers, all points whose quantitative maps were outside the range of 3*standard deviation of the mean value of each subject at each depth were excluded from the further analysis as suggested in the seminal article (Glasser and Essen, 2011) (resulting in the exclusion of less than 1%, 0.03% and 0.2% of the cortical maps of the R_1, R_2^* and χ).

For each subject, contrast and surface, spatial smoothing was performed in the inflated spherical space with a Gaussian of 2 mm width and a 6 mm radius kernel. The smoothing process was integrated with the transition from the individual space to the average subject space from freesurfer. In other words, at each point in the average space, the quantitative value was a Gaussian weighted average of the quantitative values on the existing coordinates (eroded points were not

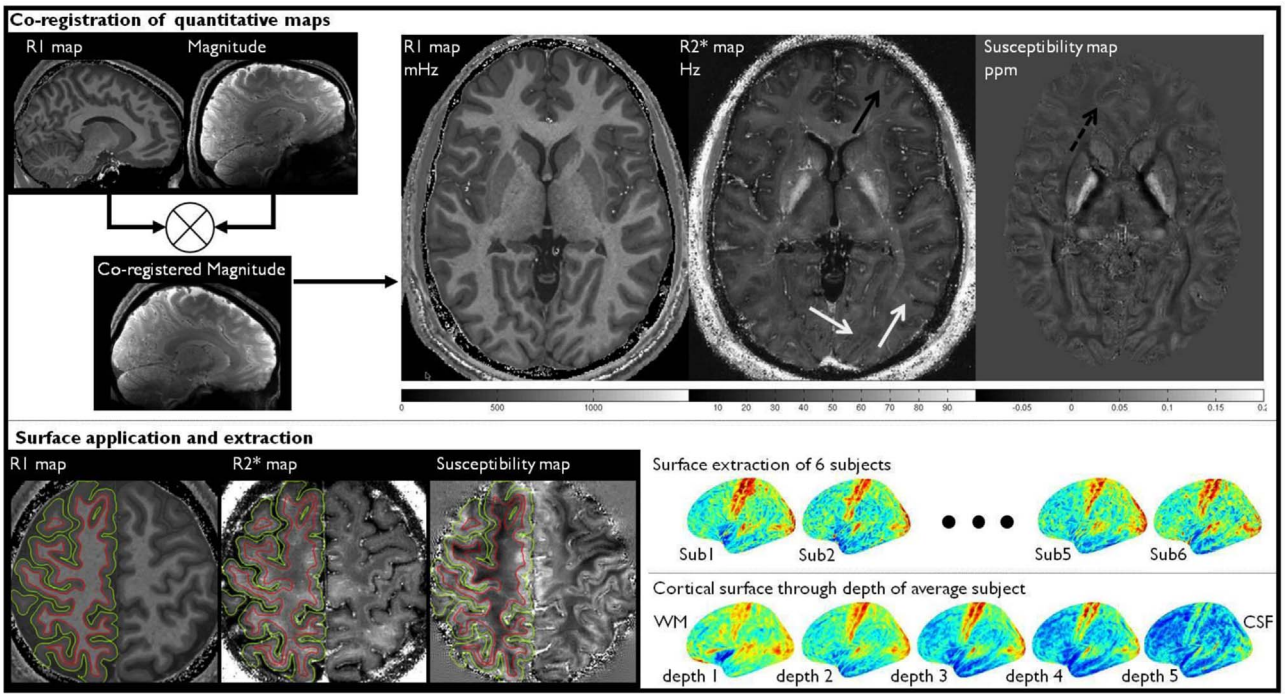

Fig. 1. The top panel shows the co-registration procedure for the three different quantitative contrasts. The magnitude image of the GRE sequence (acquired with the normal head position) is co-registered to the calculated R_1 map. This co-registration transformation is then applied to the R_2^* and QSM maps resulting in three quantitative maps perfectly aligned. Black and white arrows overlaid on the R_2^* maps highlight the varying WM/GM contrast observed on the frontal versus occipital and parietal cortices. Dashed black arrow overlaid on the susceptibility map highlights the sub-cortical paramagnetism observed in frontal white matter, which is not observed in any of the remaining contrasts. The bottom left panel shows an example of the application of the cortical surfaces computed from the R_1 maps onto the co-registered R_2^* and susceptibility maps. Red and green lines represent the GM-WM and GM-CSF borders respectively. The bottom right panel shows the R_1 cortex map from the middle surfaces for different subjects (top) and the R_1 cortex maps for different depths trough the cortex of the average subject (bottom). (For interpretation of the references to color in this figure legend, the reader is referred to the web version of this article.)

considered) of the subject specific space (with a distance smaller than 6 mm). This allowed the creation of surfaces devoid of empty vertices (either due to the background field removal erosion or the masking mentioned in the previous paragraph). Already in the average subject space, but before averaging across subjects, a single value decomposition (SVD) was applied to each quantitative contrast dataset (163842 vertices×5 cortical depths). By removing the fifth SVD component the noise was reduced while the data remained almost the same (the fifth SVD fraction of explained variance $< 1\%$ for R_1 and R_2^* maps and $< 5\%$ for susceptibility maps).

The reproducibility of the behaviour of the different layers from the inner to the outer part of the cortex was studied for all quantitative contrasts. This "through depth behaviour" in certain regions of interest (ROI) based on the main Brodmann areas, as defined in the PALS B12 atlas (Van Essen, 2005), were analysed.

Using the fsaverage coordinates in the inflated space, average quantitative contrast maps (R_1, R_2^* and susceptibility) containing different depths were created. The average maps on the fsaverage space are named average subject maps. The "through depth behaviour" in the various Brodmann areas across hemispheres was analysed.

2.4. Iron and myelin maps

If it is assumed that iron (Fe) and myelin (My) concentration are the sole contributors to the measured quantitative maps in grey matter and assuming they have a linear impact on both the relaxation parameters and susceptibility values then, the measured quantitative contrasts can be expected to have the following dependence on the concentrations of [Fe] and [My]:

$$R_1(Fe, My, BA, L) = R_{1,BL} + r_{1,Fe}*[\mathrm{Fe}(BA, L)] + r_{1,My}*[\mathrm{My}(BA, L)] \quad (4)$$

$$R_2^*(Fe, My, BA, L) = R_{2,BL}^* + r_{2,Fe}^**[\mathrm{Fe}(BA, L)] + r_{2,My}^**[\mathrm{My}(BA, L)] \quad (5)$$

$$\chi(Fe, My, BA, L) = \chi_{BL} + \chi_{Fe}*[\mathrm{Fe}(BA, L)] - \chi_{My}*[\mathrm{My}(BA, L)] \quad (6)$$

Where $R_{1,BL}$, $R_{2,BL}^*$ and χ_{BL} represent baseline values of the quantitative parameters in the absence of those perturbers, $r_{1,Fe}$ and $r_{1,My}$ are the longitunal relaxivity of iron and myelin respectively, $r_{2,Fe}^*$ and $r_{2,My}^*$ are the apparent transverse relaxivity of iron and myelin and χ_{Fe} and χ_{My} are the magnetic susceptibility of iron and myelin in ppm per concentration unit of iron and myelin. Such model has been successfully demonstrated in ex vivo experiments (Stüber et al., 2014).

In Eqs. (1)–(3), the indexes BA and L correspond to the Brodmann area and depth layer respectively. With the assumption that similar myeloarchitecture and iron concentration exists within each Brodmann area and layer, 18 ROIs (based on the Brodmann areas 1,2,3,4,6,8,9,10,17,18,19,29,30,32,41,42,44,45) at 5 different depths were used in the fitting procedure. The regions of interest were chosen to represent significantly different relaxations behaviour to better condition the problem. If only these two sources of contrast contribute to the three quantitative maps, the number of measurements is greater than the number of unknowns even when the relaxivity and baseline values are unknown, provided that the number of measurements is greater than nine. In order to increase the reliability of the fitting procedure, the iron coefficients to susceptibility (0.73×10^{-3} ppm/(mg/Kg)) and R_2^* (0.242 Hz/(mg/Kg)) were assumed as reported in Lim et al. (2013) and using the slope observed between R_2^* and susceptibility reported by Deistung et al. (2013) in deep grey matter structures at 7 T. These values are in close agreement with those obtained in other studies (Bilgic et al., 2012; Langkammer et al., 2012, 2010; Schweser et al., 2011; Wharton and Bowtell, 2013, 2010). The use of these parameters implies the calculated iron concentration will be in mg/Kg. Although various studies correlate R_1 with myelin concentration we did not find any literature with *in vivo* data at 7 T. The myelin longitudinal

relaxivity coefficient was therefore arbitrarily set to 1. Such ad-hoc definition implies an arbitrary unit to the measured myelin concentration, but is important for the stability of the fitting procedure to reduce the search space.

To avoid biasing the fitting procedure by the amplitude of the different quantitative maps ($R_2^* > R_1 > > \chi$), each of the equations was weighted by the inverse of standard deviation, of the respective quantitative measurement, across subjects (making the fitting normalized to the noise across subjects). The fitting procedure was performed using lsqfit, a non-linear solver distributed with MATLAB. The fitting problems consisted of 273 parameters (18 ROIS×5 layers×3 quantitative maps and 3 fixed relaxivity parameters) and 183 unknowns (18 ROIS×5 layers×2 tissue biomarkers and 3 free relaxivity parameters). Once the relaxivity parameters were calculated, Eqs. (4) and (5) were used to create average iron and myelin maps. This choice was made because the cortical susceptibility maps, although fundamental for the relaxivity calculation, had the larger noise particularly prior to averaging within each Brodmann area.

3. Results

3.1. Data and segmentation quality

Fig. 1 shows an outline of the processing protocol starting from the moment when the magnitude data from the gradient echo sequence gets coregistered to the R_1 space. Representative slices of the three coregistered quantitative maps are enhancing different features of the human brain and cortex. The R_1 map shows the strongest contrast between the white and gray matter, which enables the best cortical gray-white matter segmentation (and was therefore used in the freesurfer pipeline). The R_2^* map shows good vein delineation and has a grey-white matter contrast which is increased in the frontal lobe (black arrows) in comparison to the parietal (white arrows) and occipital lobe. The susceptibility map obtained with COSMOS shows white matter and significant variations of the contrast in different cortical regions: e.g. the rim of increased para-magnetism of the frontal cortex at its white matter surface (dashed back arrow); increased para-magnetism of the occipital cortex in respect to the frontal cortex is evident from increased contrast, as described in other reports at 7 T (Deistung et al., 2013).

The cortical surfaces calculated with the FreeSurfer software (green (GM-pial surface) and red (GM-WM surface) lines in Fig. 1) correspond well to the underlying R_1 contrast (from which they were calculated). The R_2^* and χ maps are by definition well co-registered between themselves (are computed from the same datasets). There is a clear agreement between the freesurfer computed outer layer (pial surface) and the R_2^* contrast, while the χ contrast in this region is significantly weaker both due to the susceptibility calculation in regions close to the brain mask and the low contrast between CSF and GM in QSM. The weak grey white-matter contrast of R_2^* maps can create the perception of mismatch with the freesurfer computed boundaries, but this can be only attributed to the different mechanisms driving the contrast.

3.2. Cortical surfaces and ROI

The cortical maps of the left hemisphere extracted from the middle layer for different subjects and quantitative contrasts is shown in Fig. 2. For all subjects, all the contrasts (but mainly R_1 and R_2^*) show similar enhanced regions, e.g. the primary motor cortex (dashed black arrow), the auditory cortex (dot-ended dashed arrow), the visual cortex (solid arrow), and the MT region (grey arrow).

Not only are the cortical maps across subjects consistent (see Fig. 1 and Fig. 2), the high resolution at which the measurements were done allowed the extraction of cortical maps at intermediate depths (see last row of Fig. 1). To show the reproducibility of the through depth behaviour of the relaxation properties across the different subjects, the mean value of the relaxation parameters in two Brodmann areas (blue: 4-somatosensory and green: 17-primary visual cortex) as a function of depth is presented in Fig. 2. Supplementary figure shows similar plots for 10 additional Brodmann regions where the interhemispheric reproducibility is also highlighted. The through layer behaviour on the R_1, R_2^* and χ was in good agreement between the six subjects and varied between different brain regions, as shown for the two Brodmann areas in Fig. 2. Interestingly, the subject's curve that has the largest deviation from the remaining subjects on the R_1 values in the somatosensory cortex (shown with a solid line) corresponds to the data that shows the largest deviation from the remaining subjects also in the visual cortex R_1 values and other brain regions (see Fig. 2 and Supplementary figure). This could have been attributed to some systematic error in the R_1 quantification due to, for example, incorrect B_1, calibration but not to local segmentation faults which would have not failed in (so many) distant brain regions. As also R_2^* and susceptibility values of this subject seem to represent outliers of our small sample, the argument of unreliable R_1 measurement should be discarded. Another potential explanation could be a small shift in the definition of the white matter and pial surface boundaries (surfaces slightly shifted to the white matter side would result in increased tissue relaxivity at all depths). The R_1 values increase of the outlier subject would suggest a misplacement of the surfaces by less than 1/5 of the local cortical thickness (corresponding to one layer on the depth scale used), such a shift would not explain the level of R_2^* increase observed for the same subject (whose R_2^* values close to the pial surface, depth 5, correspond to the remaining subjects values at depth 1–3, see Supplementary figure). Hence these differences should reflect subject specific variability of the tissue properties.

The similar behaviour of the different subjects qualifies the study of the trough depth behaviour on the average of the 6 subjects. While combining the subjects to an average subject, the information through depth of the cortex from the inner to the outer layer was kept, with Fig. 3 showing the average and standard deviations relaxation properties of 18 Brodmann regions at depth 3. These bar plot are in close agreement with other reports of R_2^* in the cortex (Cohen-Adad et al., 2012; Deistung et al., 2013). It is also possible observe that all primary sensory cortical regions (1–4, 17–19 and 41–42) have increased R_1, R_2^* and susceptibility in respect to remaining cortical regions.

All three quantitative maps show consistent through depth behaviour (see Supplementary figure) that can also be appreciated once averaged across the subjects (see Fig. 4). The behaviour differs between different ROIs and is coherent between left and right hemisphere. While the through depth behaviour of the relaxation rates (R_1 and R_2^*) show a monotonic decay from inner to outer surface, most of the susceptibility maps show a parabolic behaviour (the exception in Fig. 4 being Brodmann area 32). Both myelin and iron are known to decrease in concentration from the white matter surface to the grey matter surface (with the exception of the Baillarger bands / Gennari strip). Susceptibility contrast reflects to the average susceptibility value inside a voxel, the decrease of iron (being paramagnetic) results in a decrease of susceptibility while the decrease of myelin (being diamagnetic) leads to an increase of the susceptibility. Thus the increase in magnetic susceptibility from depth 1 to depths 2 or 3 is dominated by the iron decrease, while the decrease in susceptibility from depths 2 or 3 to depth 5 is dominated by the myelin reduction. On the other hand, the magnetic field inhomogeneities generated by each of these perturbers (iron and myelin) as a function of depth will decrease and so will the apparent relaxation rate.

3.3. Through cortex analysis

To compress the through depth information present on the quantitative maps without the need to rely on atlas based regional averaging, singular value decomposition (SVD) was performed for each quantitative contrast. The matrix to be decomposed was a rectangular

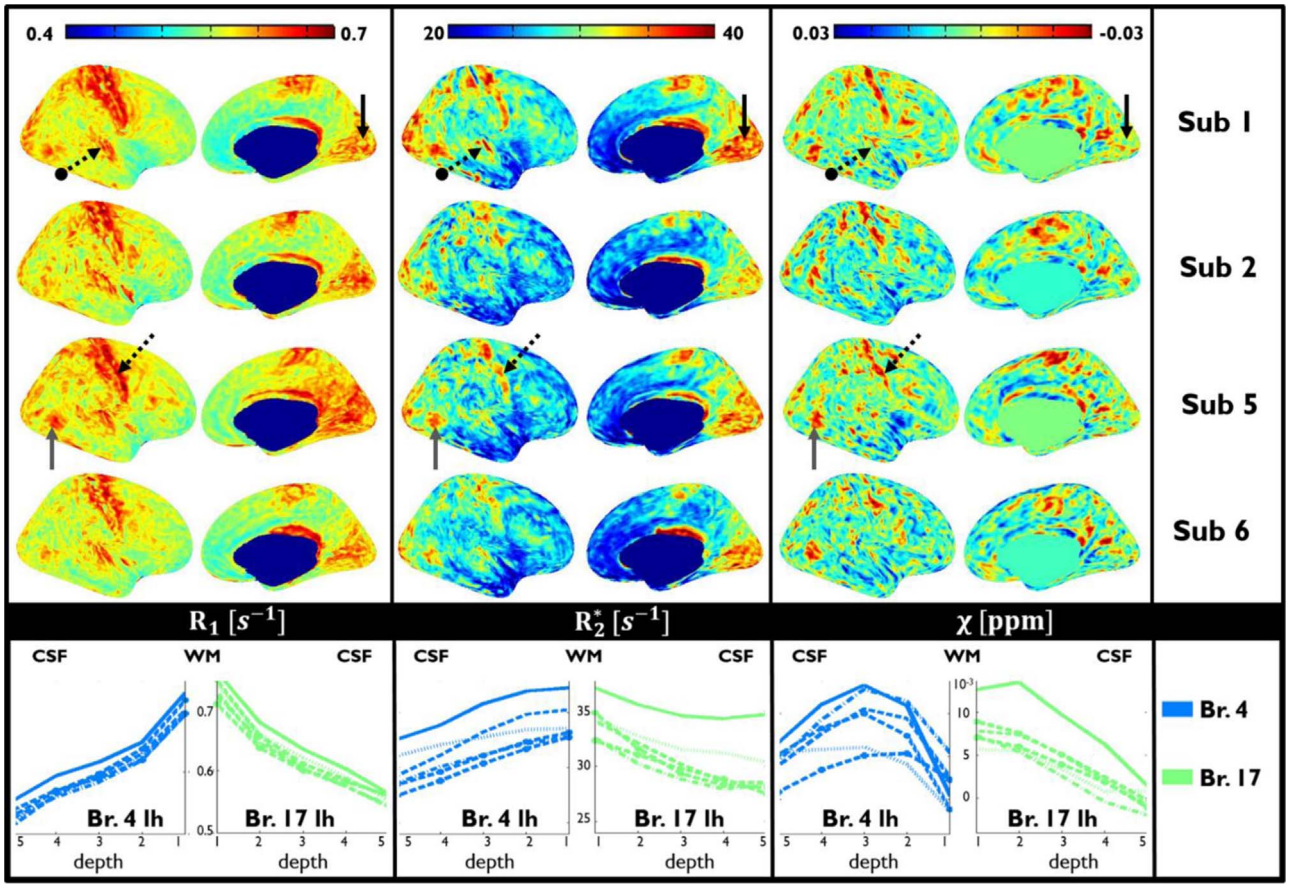

Fig. 2. The upper panel shows cortical maps of the right hemisphere obtained in the middle layer. First, second, third columns show the three quantitative contrasts (R_1,R_2^* and QSM) for different subjects (rows). Bottom panel shows plots of the different quantitative contrasts (R_1, R_2^* and χ) as a function of the layer number (depth 1 being the GM-WM surface and depth 5 closest to the pial surface) of the left hemisphere (lh) of Brodmann 4 (left) and Brodmann 17 (right) for all 6 subjects. The black arrows define different primary Brodmann areas; solid – visual cortex, dashed – motor cortex, dot-ended dashed – auditory cortex, and grey - MT region. (For interpretation of the references to color in this figure, the reader is referred to the web version of this article.)

matrix containing the $R_1/R_2^*/\chi$ values where the rows were the surface vertices and the columns the 5 different depths. The SVD decomposes a matrix in orthogonal components that explain most of the behaviour in the matrix. The first component explained most of the contrast information (98% for R_1 and R_2^* maps and 93% for the χ maps) whereas the second component points rather minor changes (2% for R_1 and R_2^* maps and 5% for χ maps) that deviate from the average behaviour while representing anatomically sensible cortical maps. The third to fifth components had no obvious anatomical features and appeared dominated by noise, suggesting that at the current SNR and spatial resolution, the through depth variations of the different contrasts can be compressed in two decay modes.

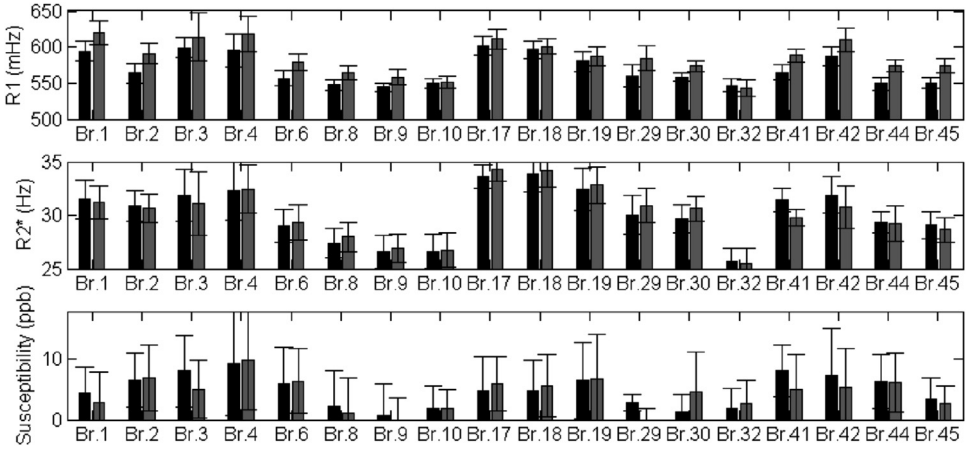

Fig. 3. Bar plots of the mean and standard deviation across subjects in 18 different Brodmann areas of the quantitative parameters: R1 (top row), R_2^* (middle row) and Magnetic Susceptibility (bottom row). The regions shown are: Br. 1–4 - Primary somatosensory and motor cortex; Br. 6, 8–10 - regions known to have decreasing density of fibers, see Nieuwenhuys (2013); Br. 17–19 - visual and supplementary-visual area; Br. 29–30 - Myelin rich retrosplenial cortex, see Glasser et al. (2011); Br. 32 - Region of Thick cortex known to gradually change into WM and reported to have low R_2^* values see Nieuwenhuys (2013), Cohen-Adad et al. (2012); Br. 41–42 - Auditory and Supplementary-Auditory regions; Br. 44–45 - Broca areas. Black and grey bars refer to the left and right hemispheres respectively.

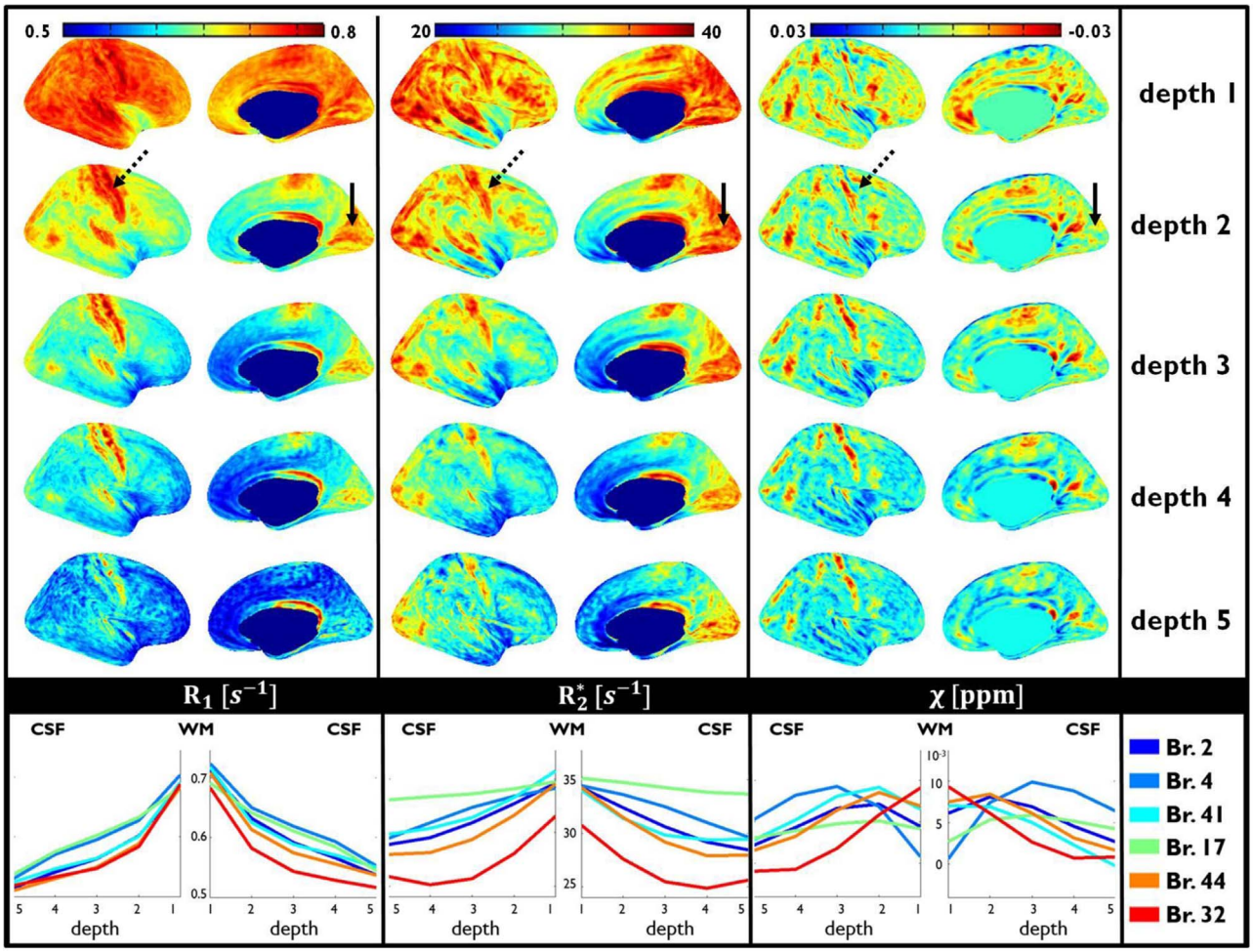

Fig. 4. First, second and third columns show the dependence on cortical depth of the R_1, R_2^* and χ respectively. Depth 1 and depth 6 (not shown) correspond to the GM-WM and the pial surface respectively. The upper panel shows cortical maps of the right hemisphere averaged across the 6 subjects at the 5 different depths. The arrows highlight: solid – visual cortex, dashed – motor cortex. Bottom panel shows, for each quantitative contrast, a plot of its variation as a function of the depth on the left (left plot) and right (right plot) hemispheres for different Brodmann areas. Brodmann regions shown: Br. 2 – somatosensory; Br. 4 - primary motor cortex; Br. 17 - primary visual cortex; Br. 41 - auditory cortex; Br. 44 - Broca's area; Br. 32 - cingulate region. (For interpretation of the references to color in this figure, the reader is referred to the web version of this article.)

The first component of the SVD (SVD_1) of R_1, R_2^* and susceptibility show similar maps (enhancing all primary sensory regions, see cortical maps in Fig. 5). The eigenvectors between left and right hemispheres were highly reproducible (see plots on Fig. 5) and represent the mean R_1, and R_2^* decay over the different layers. As already suggested by the ROI analysis in Fig. 4, the 1st component of the χ maps show a parabolic through layer variation of the magnetic susceptibility. The SVD_2 map for both R_1, and R_2^* shows as positive values (red), brain regions where the decrease of the relaxation rate is not as steep as in the remaining cortex (and negative/blue when it is steeper). The primary visual cortex appears enhanced (gray arrow in Fig. 5) in respect to neighbouring supplementary visual cortices in the second SVD component for the longitudinal and transverse relaxation rates. This can also be seen in the bar plots of Fig. 5 where Brodmann area 17 is most significantly different from areas 18 and 19 for the second component of both R_1 (suggesting a feature reminiscent of the Stria of Gennari with increased iron and myelination in the middle layers) and R_2^* (describing a slower R_2^* decay from inner to outer surface). While the R_1 contrast eigenvalue maps show both the motor and somatosensory cortex, the R_2^* and χ enhance mostly the motor cortex and show a lower enhancement of the somatosensory cortex (dot-ended arrow in Fig. 5). This behaviour is not so clear on the respective bar plots where Brodmann areas 3 and 4 are mostly equivalent. These observations suggest that quantitative maps and their profile dependence could be used for more reliable subject specific brain parcellation.

3.4. Myelin and Fe information through quantitative contrasts combination

The upper panel in Fig. 6 shows the 3 quantitative contrasts at the different brain regions and cortical depths fitted with the linear model described in Eqs. 4-6 with the following parameters:

$$R_{1,BL} = 478mHz;\ r_{1,Fe} = 6.14\frac{mHz}{mg\ /\ Kg};\ r_{1,My} = 1\frac{mHz}{au} \quad (7)$$

$$R^*_{2,BL} = 0Hz;\ r^*_{2,Fe} = 0.245\frac{Hz}{mg/Kg};\ r^*_{2,My} = 58.5\frac{Hz}{au} \quad (8)$$

$$X_{BL} = 0.14ppb;\ X_{Fe} = 0.73\frac{ppb}{mg/Kg};\ X_{My} = -340\frac{ppb}{au} \quad (9)$$

The coefficients in bold are those that were kept fixed during the fitting procedure. While the apparent transverse relaxivity of iron and its susceptibility were taken from previous studies, the longitudinal relaxivity of the diamagnetic component was arbitrarily defined to stabilize the fitting process. It is known that many of these parameters change significantly with fixation processes and temperature and hence no other values could be fixed based on literature values acquired in ex-vivo settings (Stüber et al., 2014) or other lower field iron impact on longitudinal relaxivity (Ogg and Steen, 1998). It is clear though that the model used could not satisfactorily fit all brain regions (Br. 44 and 32 was better fitted than Br. 17).

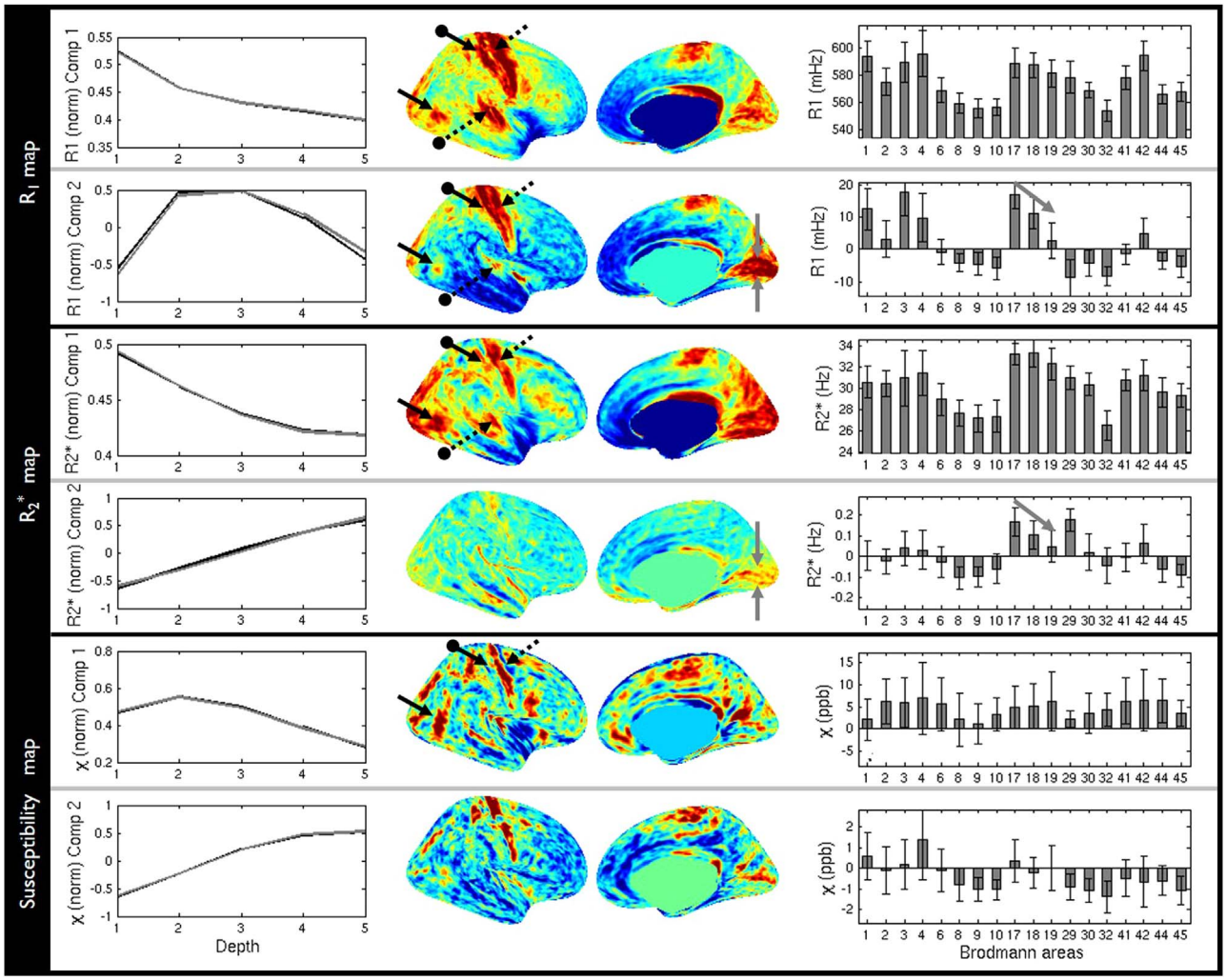

Fig. 5. shows the quantitative maps (R1 – top panel, R_2^* - middle panel and Susceptibility - bottom panel) in the cortex decomposed into two first eigenvectors across depth (top and bottom half of each panel). On the left of each sub-panel, the separately computed eigenvectors of the left and right hemisphere of the average subject are shown (black and grey lines respectively). Note that the eigenvector maps have arbitrary units, the norm of each eigenvector is 1. In the middle, the eigenvalue maps of the right hemisphere of each quantitative map and component are shown. Black arrow points to: solid – v5/MT visual area, dashed - motor cortex, dot-ended solid - somatosensory cortex, dot-ended dashed - auditory cortex. On the right, barplots of the mean value (across the region and hemispheres) of the contribution of each eigenvalue map to quantitative parameters at depth 3 are shown for 18 different Brodmann areas (error bars represent the standard deviation within each Brodmann area). The grey arrow shows the separation between primary and supplementary visual cortex that is emphasized by the second component of the R_1 and R_2^* maps.

The iron maps show increased contrast in respect to the myelin maps in all primary Brodmann regions as pointed out by the arrows in the cortical maps of Fig. 6. When looking at the through depth dependence of the computed iron and myelin distributions on the primary visual Brodmann region 17 (green) the high myelinated Stria of Gennari can be detected as a maximum on depth 4.

4. Discussion

In this paper we present quantitative R_1 and R_2^* cortical maps, in qualitative agreement with those shown by other groups (Cohen-Adad et al., 2012; Dinse et al., 2016; Sereno et al., 2013) and, for the first time, show quantitative susceptibility cortical maps that enhance similar features to those highlighted in the aforementioned relaxivity maps of the cortical surface (i.e. primary sensory regions).

The calculation of susceptibility maps using a multiple angle acquisition methodology (COSMOS) eliminates concerns from the ill posed nature of single orientation methods, yet it suffers from two potential limitations when applied to the study of the human cortex. The forward problem (Marques and Bowtell, 2005; Salomir et al., 2003) expressed on the COSMOS method assumes the validity of the sphere of Lorentz correction and the isotropic nature of the susceptibility in grey matter. In *ex vivo* experiments, these assumptions have been shown not to be valid in white matter (He and Yablonskiy, 2009; Liu et al., 2012a; Liu, 2010). The difference between longitudinal and perpendicular susceptibility of white matter in a perfectly organized optic radiation or spin cord is relatively small, 0.018–0.03 ppm (Luo et al., 2014; van Gelderen et al., 2015; Wharton and Bowtell, 2015), with the dominating anisotropic effect being that associated with its compartmentalization (Wharton and Bowtell, 2015).The amount of myelinated axons in the GM is not negligible and has been shown to cause small orientation related apparent transverse relaxation rate changes in the human cortex (Cohen-Adad et al., 2012). Modulations of R_2^* with cortex orientation in respect to the B_0 field of 1 Hz were measured in most of the cortex and up to 2–4 Hz in the primary motor, primary visual and associative auditory cortices. These values are significant smaller than the 6 Hz reported in human ex vivo hydrated tissue samples (Oh et al., 2013), 15 Hz reported in vivo in white matter of marmosets (Sati et al., 2012). This should be due not only to the reduced myelination of the cortex (in respect to white matter) but also due to the axonal arrangements in the cortex (running both parallel and perpendicular to the cortex surface) that makes it less anisotropic.

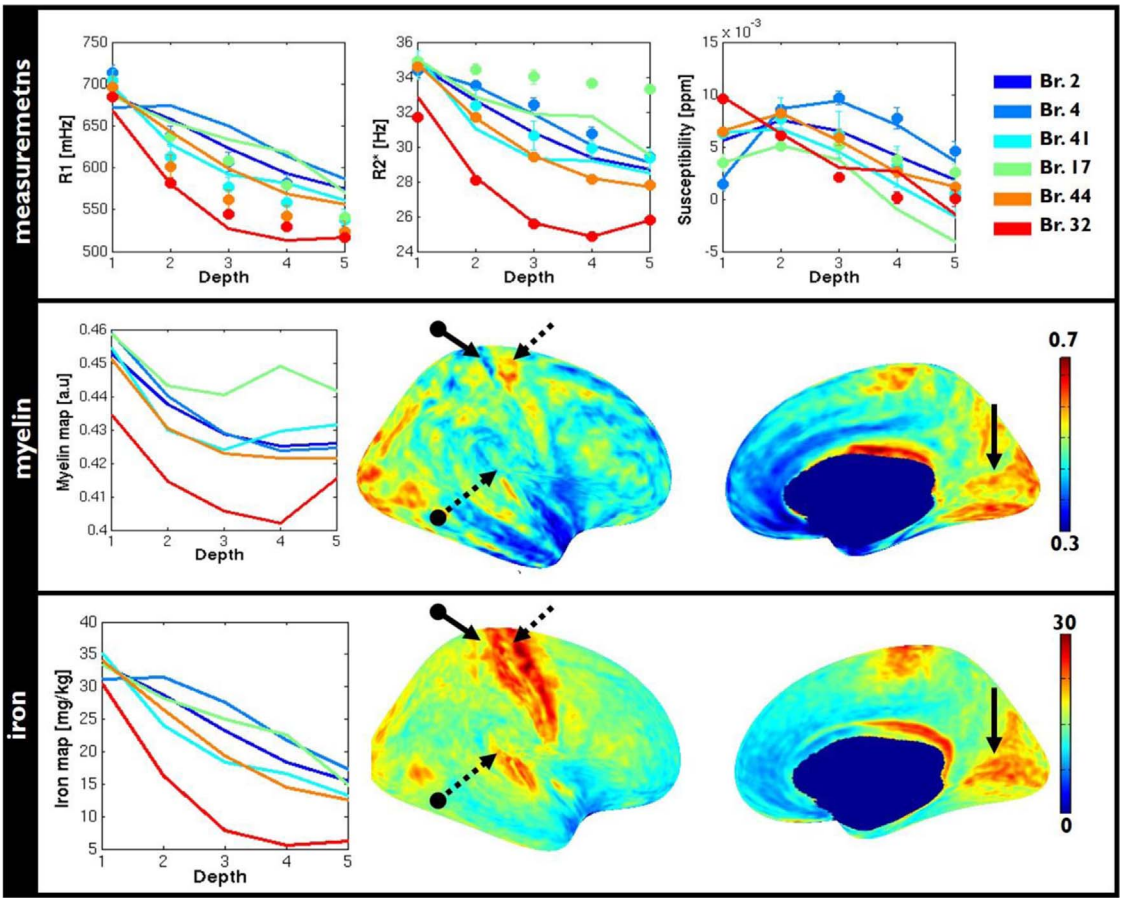

Fig. 6. Top panel shows plots of the different quantitative contrasts (R1, R_2^* and QSM) as a function of cortical depth. Measured points (circles), as well as the fitted results (solid line) are shown in each plot for different Brodmann regions: Br.2 somatosensory; Br.4 primary motor cortex; Br.17 primary visual cortex; Br. 41 auditory cortex; Br. 44 Broca's area and Br. 32 cingulate region. Plots on the left of second and third row show the computed myelin and iron distributions as a function of the depth for the Brodmann regions mentioned above. Additionally, the computed cortical maps at depth 3 of the myelin (second row) and iron (third row) distribution are shown. (For interpretation of the references to color in this figure, the reader is referred to the web version of this article.)

However, the microstructural effects described by the Generalized Lorentzian Tensor Approach (GLTA) (Yablonskiy and Sukstanskii, 2015) even if isotropically oriented (such as in GM) have a different relationship than the Lorentzian spherical cavity approach. In the GLTA approach the axial component of the susceptibility anisotropy never contributes to the averaged Lorentzian tensor (described by the COSMOS susceptibility). The other main concern when using susceptibility mapping to study the brain cortical surface is the accuracy of the background filtered field maps in the immediate neighbourhood of the brain mask. The convoluted shape of the cortex ensures that most of the cortex is fairly interior to this border. For example, all medial cortex, visual and auditory cortices are far from the edge of the brain mask due to both the hemispherical organization and the shape of the temporal lobe. Other regions such as parietal cortex, and some parts of the motor, sensory cortex could suffer from such an effect in the gyrus, but not in the fissures and sulcus which will represent the majority of the cortical surface. In this manuscript, we took advantage of the high spatial resolution achievable at high field strengths (increasing the number of pixels between edge of brain mask and pial surface), and choose a background field removal technique, based in a preliminary study (Khabipova et al., 2015), that provided filtered fieldmaps whose susceptibility maps had the expected features shown in relaxation based cortical maps. It is nevertheless expectable that there would still be room for improvement as it is apparent in the QSM slice of Fig. 1 (at the level of the motor cortex), where a remaining bias field enhancing susceptibility values in the middle section of the brain can be seen. Such bias is expected to have its origin in incomplete background field removal of one of the head position measurements and will necessarily degrade the respective cortical maps, but should have little effect on the through depth behaviour of the measured susceptibility values. One potential source of improvements would be the use of single step methods, where the background field removal of each direction is combined with the COSMOS strategy.

The high spatial resolution of our data allowed the study not only at the middle layer behaviour across the cortex, but also the “trough depth behaviour”. As a result of the choice of inversion times of the MP2RAGE sequence used to compute R_1 maps and the echo times used to calculate R_2^* maps, the relaxation rate values of CSF were not accurate. Incidentally, this layer was also missing in large parts of the susceptibility cortical maps as a result of the erosion associated with the background field removal. Hence the GM-CSF border was not taken into consideration when mapping the through depth behaviour of neither the relaxation parameters nor the susceptibility maps. Although similar behaviours were observed across subjects and, to some extent, quantitative maps (see Figs. 2–4 and Supplementary figure), for the sake of tractability of the analysis, the quantitative evaluations were performed using regions of interest associated with Brodmann areas defined on the PALS-B12 atlas (Van Essen, 2005) . This atlas, derived from T_1-weighted MRI volumes of 12 young adults, is based on the varying cytoarchitecture (rather than the varying iron concentration and the myelin content). It was nevertheless possible to observe that differences in both mean values and through depth variation of the quantitative maps (See Fig. 4) persist after this averaging process.

To better emphasize the differences between different brain regions a myelo-structure based atlas could have been more appropriate (Nieuwenhuys, 2013) as it is known that within one Brodmann region,

several myelin based regions can exist (Nieuwenhuys et al., 2014), the use of Broadman areas as ROI will tend to average out such differences. Another segmentation approach would have been automatic segmentation of the subject specific clusters for different quantitative contrasts similar to the functional parcellation of the cortex (Honnorat et al., 2015). The richness of the cortical information attained in these maps opens the door to more advanced co-registration procedures between subjects as well as its segmentation (Dinse et al., 2015). In such approaches both the spatial distribution and the through depth behaviour of the parcellated ROIs could be compared and taken into account during the transformation of the subject specific clusters to the average subject space. Fig. 5 clearly shows that, on a vertex by vertex basis, relevant cortical information exists both on the mean through cortical depth behaviour (SVD1) and the second component of the through depth behaviour (SVD2) of all the measured maps, and it could help differentiating primary and supplemental visual areas and could further contribute to individualized cortical parcellation (Glasser et al., 2016).

The through depth behaviour for each quantitative contrast was in good agreement between the different subjects, with only one subject showing significantly different behaviour for all contrasts and both hemispheres (see the example shown in Fig. 2 for Brodmann areas 4 and 17 and Supplementary figure for other Brodmann regions). Given the small population used in this study, it is not possible to statistically test any hypothesis for this outlier, yet it could be in agreement with previous reports (Callaghan et al., 2014) showing that these relaxation rates in gray matter are modulated by age (the outlier subject was 37y while remaining subjects where <29y). When creating the average subject, the analysis for the different hemispheres was kept separate. Fig. 4 thus suggests that the differences seen in through depth behaviour of R_1, R_2^* and χ are meaningful as the curves of the different Brodmann regions from the left and right hemisphere resemble in both shape and mean value. In other studies care was taken to further remove cortical surface angular dependence in respect to static magnetic field from the T^*_2 maps (Mangeat et al., 2013), while this was not performed in our analysis, it would potentially explain some of the variance observed on the T_2^* maps. The observation that χ, as opposed to R_1 and R_2^* maps does not decrease monotonically from inner surfaces to outer surfaces, suggests that myelin and iron decrease from the white matter to the pial surface at different rates. The parabolic behaviour suggests an initial faster decrease of myelin (resulting in an increase of χ) and, as it approaches the in pial surface, a faster decrease of iron concentration (resulting in a decrease of χ), which was also found by the fitting procedure of Eqs. (1)–(3), as shown in the iron and myelin plots in Fig. 6.

In this study we have tried to combine the information from in vivo quantitative R_1, R_2^* and susceptibility maps of the cortex and build iron and myelin maps of the cortex. A similar analysis, but using T^*_2 and MTR maps was able to create myelin maps using similar linear models (Mangeat et al., 2015). The model used in Eqs. (1)–(3) has shown to hold in ex vivo experiments in one single piece of cortex (Stüber et al., 2014). Yet it does not necessarily hold for different cortical sites that have different cyto- and myelo-architecture organization. For example, while it is valid to assume that the R_2^* and χ contrast are proportional to the myelin volume, this is less clear for R_1. R_1 reflects spin lattice relaxation and is linked to water mobility and could be modulated by the existing myelin surface fraction (rather than its volume). Note that the COSMOS methodology (used in this paper) might fail to characterize the true average susceptibility of the cortex namely, if the GLTA holds, it will not include the axial components of the susceptibility of inclusions. Although this term will not appear in the computed susceptibility, it will still contribute to the apparent relaxivity, creating an inconsistency between the data and the linear model used (Eqs. 1 to 3). The fits obtained (see Fig. 6) were highly dependendent on the boundary conditions, suggesting that either the quality of the susceptibility maps is not sufficient to obtain better parameterization of $r_{1,My}$, $r_{1,Fe}$, $r^*_{2,My}$, $r^*_{2,Fe}$, χ_{My}, χ_{Fe} (the problem is ill-conditioned if some other of these parameters are not fixed) or the model suggested is not valid across the cortex because the baseline susceptibility or relaxivity values might vary throughout the brain (which is something not tested ex-vivo). While the resulting iron and myelin profiles in different cortical areas could be explained by some known anatomical landmarks (Nieuwenhuys et al., 2014), the resulting cortical maps have features that contradict the expected myelin maps. The most striking observation being that it is the paramagnetic/iron map that retained most of the features observed in the R_1 maps. This suggests that more work will have to be conducted in finding better models that could bring together these quantitative maps, or that further improvements are needed in the computation of quantitative maps and calibration of the various equation parameters.

5. Conclusion

The cortical R_1, R_2^* and susceptibility maps show similar contrast to those reported by other groups with the cortical maps showing an enhancement of primary Broadmann regions. The behaviour from the inner layer, close to the WM border, to the outer layer, close to the pial surface, for each contrast is coherent between the left and right hemisphere, demonstrating the reproducibility of these results. The through depth behaviour information in R_1 maps could be useful for subject specific cortical parcellation. While the combination of information of R_1 and R_2^* cortical maps offers the potential to obtain myelin/diamagnetic cortical maps clean of, amongst other, iron/paramagnetic contributions (and vice versa), more work is needed to better parameterize and model the contribution of each perturber to the quantitative maps.

Acknowledgements

This work was supported by Centre d'Imagerie BioMédicale (CIBM) of the UNIL, UNIGE, HUG, CHUV, EPFL and the Leenaards and Louis-Jeantet Foundations. The authors would like to thank Daniel Gallichan for sequence development support, Tim van Mourik for providing the software to calculate equi-volume depth segmentation of the cortical maps, Jonathan Polimeni for providing freesurfer scripts able to use the high spatial resolution MP2RAGE data and Marc Remy for IT support. D.K. and this project were funded by the Swiss National Science Foundation (SNF) grant No 132821.

Appendix A. Supplementary material

Supplementary data associated with this article can be found in the online version at http://dx.doi.org/10.1016/j.neuroimage.2016.12.009.

References

Bilgic, B., Pfefferbaum, A., Rohlfing, T., Sullivan, E.V., Adalsteinsson, E., 2012. MRI estimates of brain iron concentration in normal aging using quantitative susceptibility mapping. NeuroImage 59, 2625–2635. http://dx.doi.org/10.1016/j.neuroimage.2011.08.077.

Bock, N.A., Kocharyan, A., Liu, J.V., Silva, A.C., 2009. Visualizing the entire cortical myelination pattern in marmosets with magnetic resonance imaging. J. Neurosci. Methods 185, 15–22. http://dx.doi.org/10.1016/j.jneumeth.2009.08.022.

Bot, J.C.J., Blezer, E.L.A., Kamphorst, W., Lycklama à Nijeholt, G.J., Ader, H.J., Castelijns, J.A., Ig, K.N., Bergers, E., Ravid, R., Polman, C., Barkhof, F., 2004. The spinal cord in multiple sclerosis: relationship of high-spatial-resolution quantitative mr imaging findings to histopathologic results. Radiology 233, 531–540. http://dx.doi.org/10.1148/radiol.2332031572.

Brodmann, K., 1909. Vergleichende Lokalisationslehre der Grosshirnrinde in ihren Prinzipien dargestellt auf Grund des Zellenbaues. Leipzig.

Callaghan, M.F., Freund, P., Draganski, B., Anderson, E., Cappelletti, M., Chowdhury, R., Diedrichsen, J., FitzGerald, T.H.B., Smittenaar, P., Helms, G., Lutti, A., Weiskopf, N., 2014. Widespread age-related differences in the human brain microstructure revealed by quantitative magnetic resonance imaging. Neurobiol. Aging 35, 1862–1872. http://dx.doi.org/10.1016/j.neurobiolaging.2014.02.008.

Cohen-Adad, J., Polimeni, J.R., Helmer, K.G., Benner, T., McNab, J.A., Wald, L.L., Rosen, B.R., Mainero, C., 2012. T2* mapping and B0 orientation-dependence at 7 T reveal cyto- and myeloarchitecture organization of the human cortex. NeuroImage 60, 1006–1014. http://dx.doi.org/10.1016/j.neuroimage.2012.01.053.

Cramer, S.C., Sur, M., Dobkin, B.H., O'Brien, C., Sanger, T.D., Trojanowski, J.Q., Rumsey, J.M., Hicks, R., Cameron, J., Chen, D., Chen, W.G., Cohen, L.G., deCharms, C., Duffy, C.J., Eden, G.F., Fetz, E.E., Filart, R., Freund, M., Grant, S.J., Haber, S., Kalivas, P.W., Kolb, B., Kramer, A.F., Lynch, M., Mayberg, H.S., McQuillen, P.S., Nitkin, R., Pascual-Leone, A., Reuter-Lorenz, P., Schiff, N., Sharma, A., Shekim, L., Stryker, M., Sullivan, E.V., Vinogradov, S., 2011. Harnessing neuroplasticity for clinical applications. Brain 134, 1591–1609. http://dx.doi.org/10.1093/brain/awr039.

Deistung, A., Schäfer, A., Schweser, F., Biedermann, U., Turner, R., Reichenbach, J.R., 2013. Toward in vivo histology: a comparison of quantitative susceptibility mapping (QSM) with magnitude-, phase-, and R2*-imaging at ultra-high magnetic field strength. NeuroImage 65, 299–314. http://dx.doi.org/10.1016/j.neuroimage.2012.09.055.

Dick, F., Tierney, A.T., Lutti, A., Josephs, O., Sereno, M.I., Weiskopf, N., 2012. In vivo functional and myeloarchitectonic mapping of human primary auditory areas. J. Neurosci. 32, 16095–16105. http://dx.doi.org/10.1523/JNEUROSCI.1712-12.2012.

Dinse, J., Härtwich, N., Waehnert, M.D., Tardif, C.L., Schäfer, A., Geyer, S., Preim, B., Turner, R., Bazin, P.-L., 2015. A cytoarchitecture-driven myelin model reveals area-specific signatures in human primary and secondary areas using ultra-high resolution in-vivo brain MRI. NeuroImage 114, 71–87. http://dx.doi.org/10.1016/j.neuroimage.2015.04.023.

Duyn, J.H., van Gelderen, P., Li, T.-Q., de Zwart, J.A., Koretsky, A.P., Fukunaga, M., 2007. High-field MRI of brain cortical substructure based on signal phase. Proc. Natl. Acad. Sci. U.S.A. 104, 11796–11801. http://dx.doi.org/10.1073/pnas.0610821104.

Eggenschwiler, F., Kober, T., Magill, A.W., Gruetter, R., Marques, J.P., 2012. SA2RAGE: a new sequence for fast B1 +-mapping. Magn. Reson. Med. 67, 1609–1619. http://dx.doi.org/10.1002/mrm.23145.

Fischl, B., Salat, D.H., Busa, E., Albert, M., Dieterich, M., Haselgrove, C., van der Kouwe, A., Killiany, R., Kennedy, D., Klaveness, S., Montillo, A., Makris, N., Rosen, B., Dale, A.M., 2002. Whole brain segmentation: automated labeling of neuroanatomical structures in the human brain. Neuron 33, 341–355. http://dx.doi.org/10.1016/S0896-6273(02)00569-X.

Fischl, B., Salat, D.H., van der Kouwe, A.J.W., Makris, N., Ségonne, F., Quinn, B.T., Dale, A.M., 2004. Sequence-independent segmentation of magnetic resonance images. NeuroImage Math. Brain Imaging 23 (Supplement 1), S69–S84. http://dx.doi.org/10.1016/j.neuroimage.2004.07.016.

Geyer, S., Weiss, M., Reimann, K., Lohmann, G., Turner, R., 2011. Microstructural parcellation of the human cerebral cortex – from Brodmann's post-mortem map to in vivo mapping with high-field magnetic resonance imaging. Front. Hum. Neurosci. 5, 19. http://dx.doi.org/10.3389/fnhum.2011.00019.

Glasser, M.F., Essen, D.C.V., 2011. Mapping human cortical areas in vivo based on myelin content as revealed by T1- and T2-weighted MRI. J. Neurosci. 31, 11597–11616. http://dx.doi.org/10.1523/JNEUROSCI.2180-11.2011.

Glasser, M.F., Coalson, T.S., Robinson, E.C., Hacker, C.D., Harwell, J., Yacoub, E., Ugurbil, K., Andersson, J., Beckmann, C.F., Jenkinson, M., Smith, S.M., Van Essen, D.C., 2016. A multi-modal parcellation of human cerebral cortex. Nature 536, 171–178. http://dx.doi.org/10.1038/nature18933.

Haacke, E.M., Cheng, N.Y.C., House, M.J., Liu, Q., Neelavalli, J., Ogg, R.J., Khan, A., Ayaz, M., Kirsch, W., Obenaus, A., 2005. Imaging iron stores in the brain using magnetic resonance imaging. Magn. Reson. Imaging 23, 1–25. http://dx.doi.org/10.1016/j.mri.2004.10.001.

He, X., Yablonskiy, D.A., 2009. Biophysical mechanisms of phase contrast in gradient echo MRI. Proc. Natl. Acad. Sci. U.S.A. 106, 13558–13563. http://dx.doi.org/10.1073/pnas.0904899106.

Honnorat, N., Eavani, H., Satterthwaite, T.D., Gur, R.E., Gur, R.C., Davatzikos, C., 2015. GraSP: geodesic graph-based segmentation with shape priors for the functional parcellation of the cortex. NeuroImage 106, 207–221. http://dx.doi.org/10.1016/j.neuroimage.2014.11.008.

Hopf, A., Gräfin Vitzthum, H., 1957. Über die verteilung myeloarchitektonischer merkmale in der scheitellappenrinde beim menschen - HopfAdolf2.pdf. J. Hirnforsch. 3.

Hopp, K., Popescu, B.F.G., McCrea, R.P.E., Harder, S.L., Robinson, C.A., Haacke, M.E., Rajput, A.H., Rajput, A., Nichol, H., 2010. Brain iron detected by SWI high pass filtered phase calibrated with synchrotron X-ray fluorescence. J. Magn. Reson. Imaging 31, 1346–1354. http://dx.doi.org/10.1002/jmri.22201.

Khabipova, D., Wiaux, Y., Gruetter, R., Marques, J.P., 2015. A modulated closed form solution for quantitative susceptibility mapping — A thorough evaluation and comparison to iterative methods based on edge prior knowledge. NeuroImage 107, 163–174. http://dx.doi.org/10.1016/j.neuroimage.2014.11.038.

Kleinnijenhuis, M., van Mourik, T., Norris, D.G., Ruiter, D.J., van Cappellen van Walsum, A.-M., Barth, M., 2015. Diffusion tensor characteristics of gyrencephaly using high resolution diffusion MRI in vivo at 7T. NeuroImage 109, 378–387. http://dx.doi.org/10.1016/j.neuroimage.2015.01.001.

Kleist, K., 1937. Bericht über die gehirnpathologie in ihrer bedeutung für neurologie und psychiatrie. Z. Für Gesamte Neurol. Psychiatr. 158, 159–193. http://dx.doi.org/10.1007/BF02870728.

Langkammer, C., Krebs, N., Goessler, W., Scheurer, E., Ebner, F., Yen, K., Fazekas, F., Ropele, S., 2010. Quantitative MR imaging of brain iron: a postmortem validation study. Radiology 257, 455–462. http://dx.doi.org/10.1148/radiol.10100495.

Langkammer, C., Schweser, F., Krebs, N., Deistung, A., Goessler, W., Scheurer, E., Sommer, K., Reishofer, G., Yen, K., Fazekas, F., Ropele, S., Reichenbach, J.R., 2012. Quantitative susceptibility mapping (QSM) as a means to measure brain iron? A post mortem validation study. NeuroImage 62, 1593–1599. http://dx.doi.org/10.1016/j.neuroimage.2012.05.049.

Lim, I.A.L., Faria, A.V., Li, X., Hsu, J.T.C., Airan, R.D., Mori, S., van Zijl, P.C.M., 2013. Human brain atlas for automated region of interest selection in quantitative susceptibility mapping: application to determine iron content in deep gray matter structures. NeuroImage 82, 449–469. http://dx.doi.org/10.1016/j.neuroimage.2013.05.127.

Liu, C., 2010. Susceptibility tensor imaging. Magn. Reson. Med.: Off. J. Soc. Magn. Reson. Med. Soc. Magn. Reson. Med. 63, 1471–1477. http://dx.doi.org/10.1002/mrm.22482.

Liu, C., Li, W., Johnson, G.A., Wu, B., 2011. High-field (9.4 T) MRI of brain dysmyelination by quantitative mapping of magnetic susceptibility. NeuroImage 56, 930–938. http://dx.doi.org/10.1016/j.neuroimage.2011.02.024.

Liu, C., Li, W., Wu, B., Jiang, Y., Johnson, G.A., 2012a. 3D fiber tractography with susceptibility tensor imaging. NeuroImage 59, 1290–1298. http://dx.doi.org/10.1016/j.neuroimage.2011.07.096.

Liu, T., Spincemaille, P., de Rochefort, L., Kressler, B., Wang, Y., 2009. Calculation of susceptibility through multiple orientation sampling (COSMOS): a method for conditioning the inverse problem from measured magnetic field map to susceptibility source image in MRI. Magn. Reson. Med.: Off. J. Soc. Magn. Reson. Med. Soc. Magn. Reson. Med. 61, 196–204. http://dx.doi.org/10.1002/mrm.21828.

Lodygensky, G.A., Marques, J.P., Maddage, R., Perroud, E., Sizonenko, S.V., Hüppi, P.S., Gruetter, R., 2012. In vivo assessment of myelination by phase imaging at high magnetic field. NeuroImage 59, 1979–1987. http://dx.doi.org/10.1016/j.neuroimage.2011.09.057.

Luo, J., He, X., Yablonskiy, D.A., 2014. Magnetic susceptibility induced white matter MR signal frequency shifts—experimental comparison between Lorentzian sphere and generalized Lorentzian approaches. Magn. Reson. Med. 71, 1251–1263. http://dx.doi.org/10.1002/mrm.24762.

Mangeat, G., Govindarajan, S.T., Mainero, C., Cohen-Adad, J., 2015. Multivariate combination of magnetization transfer, T2* and B0 orientation to study the myelo-architecture of the in vivo human cortex. NeuroImage 119, 89–102. http://dx.doi.org/10.1016/j.neuroimage.2015.06.033.

Marques, J.P., Bowtell, R., 2005. Application of a fourier-based method for rapid calculation of field inhomogeneity due to spatial variation of magnetic susceptibility. Concepts Magn. Reson. Part B Magn. Reson. Eng. 25, 65–78. http://dx.doi.org/10.1002/cmr.b.20034.

Marques, J.P., Gruetter, R., 2013. New developments and applications of the MP2RAGE sequence - focusing the contrast and high spatial resolution R1 mapping. PLoS ONE 8. http://dx.doi.org/10.1371/journal.pone.0069294.

Marques, J.P., Kober, T., Krueger, G., van der Zwaag, W., Van de Moortele, P.-F., Gruetter, R., 2010. MP2RAGE, a self bias-field corrected sequence for improved segmentation and T1-mapping at high field. NeuroImage 49, 1271–1281. http://dx.doi.org/10.1016/j.neuroimage.2009.10.002.

McRae, R., Bagchi, P., Sumalekshmy, S., Fahrni, C.J., 2009. In situ imaging of metals in cells and tissues. Chem. Rev. 109, 4780–4827. http://dx.doi.org/10.1021/cr900223a.

Morawski, M., Meinecke, C., Reinert, T., Dörffel, A.C., Riederer, P., Arendt, T., Butz, T., 2005. Determination of trace elements in the human substantia nigra. Nucl. Instrum. Methods Phys. Res. Sect. B Beam Interact. Mater. At., Nuclear Microprobe Technology and Applications. In: Proceedings of the 9th International Conference on Nuclear Microprobe Technology and Applications. 231, pp. 224–228. ⟨http://dx.doi.org/10.1016/j.nimb.2005.01.061⟩

Mottershead, J.P., Schmierer, K., Clemence, M., Thornton, J.S., Scaravilli, F., Barker, G.J., Tofts, P.S., Newcombe, J., Cuzner, M.L., Ordidge, R.J., McDonald, W.I., Miller, P.D.H., 2003. High field MRI correlates of myelin content and axonal density in multiple sclerosis. J. Neurol. 250, 1293–1301. http://dx.doi.org/10.1007/s00415-003-0192-3.

Nieuwenhuys, R., 2013. The myeloarchitectonic studies on the human cerebral cortex of the Vogt–Vogt school, and their significance for the interpretation of functional neuroimaging data. Brain Struct. Funct. 218, 303–352. http://dx.doi.org/10.1007/s00429-012-0460-z.

Nieuwenhuys, R., Broere, C.A.J., Cerliani, L., 2014. A new myeloarchitectonic map of the human neocortex based on data from the Vogt–Vogt school. Brain Struct. Funct. 220, 2551–2573. http://dx.doi.org/10.1007/s00429-014-0806-9.

Ogg, R.J., Steen, R.G., 1998. Age-related changes in brain T1 are correlated with iron concentration. Magn. Reson. Med. 40, 749–753.

Oh, S.-H., Kim, Y.-B., Cho, Z.-H., Lee, J., 2013. Origin of B0 orientation dependent R2* (=1/T2*) in white matter. NeuroImage 73, 71–79. http://dx.doi.org/10.1016/j.neuroimage.2013.01.051.

de Rochefort, L., Wand, H., Loureiro de Sousa, P., Armspach, J., 2013. Efficient and Automatic Harmonic Field Pre-Filtering for Brain Quantitative Susceptibility Mapping. In: Proceedings of the ISMRM. Presented at the Annual Meeting of the International Society for Magnetitic Reasonance in Medicine, Salt Lake City, Utah, USA, p. 170.

Rooney, W.D., Johnson, G., Li, X., Cohen, E.R., Kim, S.-G., Ugurbil, K., Springer, C.S., 2007. Magnetic field and tissue dependencies of human brain longitudinal 1H2O relaxation in vivo. Magn. Reson. Med. 57, 308–318. http://dx.doi.org/10.1002/mrm.21122.

Salomir, R., de Senneville, B.D., Moonen, C.T., 2003. A fast calculation method for magnetic field inhomogeneity due to an arbitrary distribution of bulk susceptibility. Concepts Magn. Reson. Part B Magn. Reson. Eng. 19B, 26–34. http://dx.doi.org/10.1002/cmr.b.10083.

Sarkissov, S.A., Filimonoff, I.N., Kononowa, E.P., Preobraschenskaja, I.S., Kukuew, L.A.,

1955. Atlas of the cytoarchitectonics of the human cerebral cortex. Medgiz, Moscow.
Sati, P., Silva, A.C., van Gelderen, P., Gaitan, M.I., Wohler, J.E., Jacobson, S., Duyn, J.H., Reich, D.S., 2012. In vivo quantification of T2* anisotropy in white matter fibers in marmoset monkeys. NeuroImage 59, 979–985. http://dx.doi.org/10.1016/j.neuroimage.2011.08.064.
Schmierer, K., Scaravilli, F., Altmann, D.R., Barker, G.J., Miller, D.H., 2004. Magnetization transfer ratio and myelin in postmortem multiple sclerosis brain. Ann. Neurol. 56, 407–415. http://dx.doi.org/10.1002/ana.20202.
Schweser, F., Deistung, A., Lehr, B.W., Reichenbach, J.R., 2011. Quantitative imaging of intrinsic magnetic tissue properties using MRI signal phase: an approach to in vivo brain iron metabolism? NeuroImage 54, 2789–2807. http://dx.doi.org/10.1016/j.neuroimage.2010.10.070.
Schweser, F., Robinson, S.D., de Rochefort, L., Li, W., Bredies, K., 2016. An illustrated comparison of processing methods for phase MRI and QSM: removal of background field contributions from sources outside the region of interest. NMR Biomed.. http://dx.doi.org/10.1002/nbm.3604.
Sereno, M.I., Lutti, A., Weiskopf, N., Dick, F., 2013. Mapping the Human Cortical Surface by Combining Quantitative T1 with Retinotopy. Cereb. Cortex 23, 2261–2268. http://dx.doi.org/10.1093/cercor/bhs213.
Sigalovsky, I.S., Fischl, B., Melcher, J.R., 2006. Mapping an intrinsic MR property of gray matter in auditory cortex of living humans: a possible marker for primary cortex and hemispheric differences. NeuroImage 32, 1524–1537. http://dx.doi.org/10.1016/j.neuroimage.2006.05.023.
Stüber, C., Morawski, M., Schäfer, A., Labadie, C., Wähnert, M., Leuze, C., Streicher, M., Barapatre, N., Reimann, K., Geyer, S., Spemann, D., Turner, R., 2014. Myelin and iron concentration in the human brain: a quantitative study of MRI contrast. NeuroImage 93 (Pt 1), 95–106. http://dx.doi.org/10.1016/j.neuroimage.2014.02.026.
Toga, A.W., Thompson, P.M., Mori, S., Amunts, K., Zilles, K., 2006. Towards multimodal atlases of the human brain. Nat. Rev. Neurosci. 7, 952–966. http://dx.doi.org/10.1038/nrn2012.
Van Essen, D.C., 2005. A population-average, landmark- and surface-based (PALS) atlas of human cerebral cortex. NeuroImage 28, 635–662. http://dx.doi.org/10.1016/j.neuroimage.2005.06.058.
van Gelderen, P., Mandelkow, H., de Zwart, J.A., Duyn, J.H., 2015. A torque balance measurement of anisotropy of the magnetic susceptibility in white matter. Magn. Reson. Med. 74, 1388–1396. http://dx.doi.org/10.1002/mrm.25524.
Vogt, C., Vogt, O., 1919. Allgemeinere ergebnisse unserer hirnforschung. J. Psychol. Neurol. 25, 292–398.
von Economo, C., Koskinas, G.N., 1925. Die Cytoarchitektonik der Hirnrinde des erwachsenen Menschen.. Springer, Wien.
Wang, Y., Liu, T., 2015. Quantitative susceptibility mapping (QSM): decoding MRI data for a tissue magnetic biomarker. Magn. Reson. Med. 73, 82–101. http://dx.doi.org/10.1002/mrm.25358.
Wharton, S., Bowtell, R., 2010. Whole-brain susceptibility mapping at high field: a comparison of multiple- and single-orientation methods. NeuroImage 53, 515–525. http://dx.doi.org/10.1016/j.neuroimage.2010.06.070.
Wharton, S., Bowtell, R., 2013. Gradient echo based fiber orientation mapping using R2* and frequency difference measurements. NeuroImage 83, 1011–1023. http://dx.doi.org/10.1016/j.neuroimage.2013.07.054.
Wharton, S., Bowtell, R., 2015. Effects of white matter microstructure on phase and susceptibility maps. Magn. Reson. Med. 73, 1258–1269. http://dx.doi.org/10.1002/mrm.25189.
Wharton, S., Schäfer, A., Bowtell, R., 2010. Susceptibility mapping in the human brain using threshold-based k-space division. Magn. Reson. Med.: Off. J. Soc. Magn. Reson. Med. Soc. Magn. Reson. Med. 63, 1292–1304. http://dx.doi.org/10.1002/mrm.22334.
Yablonskiy, D.A., Sukstanskii, A.L., 2015. Generalized Lorentzian Tensor Approach (GLTA) as a biophysical background for quantitative susceptibility mapping. Magn. Reson. Med. 73, 757–764. http://dx.doi.org/10.1002/mrm.25538.
Yablonskiy, D.A., Luo, J., Sukstanskii, A.L., Iyer, A., Cross, A.H., 2012. Biophysical mechanisms of MRI signal frequency contrast in multiple sclerosis. Proc. Natl. Acad. Sci. U.S.A. 109, 14212–14217. http://dx.doi.org/10.1073/pnas.1206037109.
Zheng, W., Nichol, H., Liu, S., Cheng, Y.-C.N., Haacke, E.M., 2013. Measuring iron in the brain using quantitative susceptibility mapping and X-ray fluorescence imaging. NeuroImage 78, 68–74. http://dx.doi.org/10.1016/j.neuroimage.2013.04.022.
Zilles, K., Amunts, K., 2009. Receptor mapping: architecture of the human cerebral cortex. Curr. Opin. Neurol. 22, 331–339. http://dx.doi.org/10.1097/WCO.0b013e32832d95db.
Zilles, K., Amunts, K., 2010. Centenary of Brodmann's map — conception and fate. Nat. Rev. Neurosci. 11, 139–145. http://dx.doi.org/10.1038/nrn2776.
Zilles, K., Palomero-Gallagher, N., Grefkes, C., Scheperjans, F., Boy, C., Amunts, K., Schleicher, A., 2002. Architectonics of the human cerebral cortex and transmitter receptor fingerprints: reconciling functional neuroanatomy and neurochemistry. Eur. Neuropsychopharmacol. 12, 587–599. http://dx.doi.org/10.1016/S0924-977X(02)00108-6.